# Viscoelastic confinement induces periodic flow reversals in active nematics

Francesco Mori [,1] Saraswat Bhattacharyya,[1] Julia M. Yeomans [,1] and Sumesh P. Thampi [2]

[1]*Rudolf Peierls Centre for Theoretical Physics, University of Oxford, Oxford OX1 3PU, United Kingdom*
[2]*Department of Chemical Engineering, Indian Institute of Technology Madras, Chennai-36, India*

We use linear stability analysis and hybrid lattice Boltzmann simulations to study the dynamical behavior of an active nematic confined in a channel made of viscoelastic material. We find that the quiescent, ordered active nematic is unstable above a critical activity. The transition is to a steady flow state for high elasticity of the channel surroundings. However, below a threshold elastic modulus, the system produces spontaneous oscillations with periodic flow reversals. We provide a phase diagram that highlights the region where time-periodic oscillations are observed and explain how they are produced by the interplay of activity and viscoelasticity. Our results suggest experiments to study the role of viscoelastic confinement in the spatiotemporal organization and control of active matter.

## I. INTRODUCTION

Living systems across scales exhibit collective motion and thus spatiotemporal patterns, vividly manifested as, for instance, motility-induced phase separation [1], spontaneous flow transitions [2–5], and turbulence at low Reynolds number [6–8]. Not only biochemical and genetic cues but mechanical interactions of the system with its surroundings are important in dictating such emergent dynamics. Adding to this complexity, biological environments are often endowed with viscoelastic properties, for example, biofilms where bacterial cells colonize in a polymeric matrix [9], migration of cells through extracellular matrix [10–13], notably the phenomenon of durotaxis [14], and change in the swimming behavior of microorganisms due to the presence of polymers in biofluids [15,16]. In a different context, traction force microscopy has become an indispensable tool to probe force fields in cellular structures. The technique assumes a one-way mechanical interaction of cells with an elastic substrate [17,18]. Therefore, clarifying the interplay of the viscoelasticity of a confining medium and activity of the living system is crucial from understanding measurements in mechanobiology to biological events such as wound healing [19], morphogenesis [20], and cancer invasion [21]. Besides, identifying universal pathways of pattern formation is a central goal of active matter research.

It is well known that active nematics, a versatile model fluid for active matter, confined in a rigid channel displays a transition—mathematically analogous to the Fredericks transition in passive liquid crystals [22]—from quiescence to a flow state when the activity is increased beyond a threshold

value [2,23–26]. Further increase in activity induces a cascade of dynamical transitions resulting in oscillatory flows [4,27], dancing topological defects [27,28], and active turbulence [29–33]. In addition, recent experiments have employed microfluidic technologies to control and generate complex fluxes in active nematics [34,35]. Thus channel-confined active nematics have become a paradigm for understanding the dynamical behavior of active systems [36]. Therefore, we investigate the interaction between activity and viscoelasticity by analyzing an active nematic flowing in a soft channel.

Previous studies that address the role of viscoelasticity in living systems considered either active particles within a viscoelastic fluid [37–42] or active matter in contact with a viscoelastic environment [43–45]. In the former case, oscillating vortices and drag reduction effects are seen to arise due to the presence of polymers [40,41]. In the latter, less studied case, numerical simulations demonstrate that temporal pulses in activity drive reversal of spontaneous flows [44]. Moreover, spontaneous flow reversals have been experimentally observed in swimming bacteria confined in a disk [46]. In this paper, we demonstrate analytically and numerically that, above a critical activity, viscoelastic confinement produces spontaneous, oscillatory flow states of an active nematic that switches flow directions periodically. The direction-reversing oscillatory flows exist only in "soft" channels and they disappear when the elastic modulus of the confinement increases above a critical value. Building on our findings, we explain the origin of oscillations as the interplay of activity and viscoelasticity, demonstrate the generality of the phenomenon, and discuss the consequences.

## II. MODEL

We consider a two-dimensional channel of width $2L$ and infinite length which contains the active nematic. The borders of the channel which span a width of $(\beta - 1)L$ on either
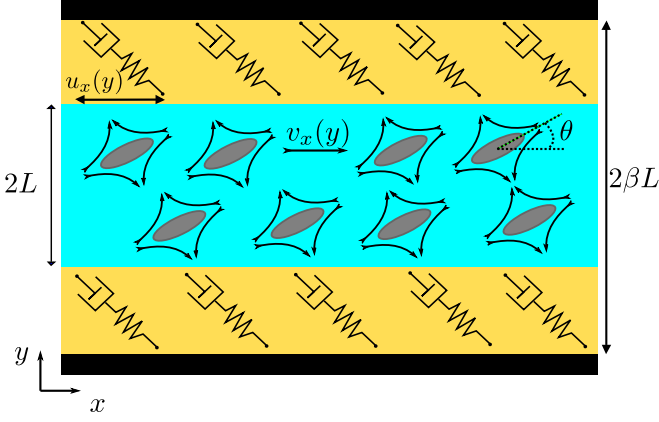
FIG. 1. Schematic representation of the system: an active nematic layer of width $2L$ is confined between two viscoelastic layers, each of width $(\beta - 1)L$. Thus the bounding rigid plates are separated by a distance $2\beta L$. The active nematic is a dense suspension of elements that generate active stress. The viscoelastic layers are shown as made up of Maxwell elements.

side are made up of viscoelastic material (see Fig. 1). Let $x$ and $y$ denote the directions parallel and perpendicular to the channel length, with $y = 0$ the center line of the channel. The relevant hydrodynamic variables are $\mathbf{Q}$ and $\boldsymbol{v}$ representing the orientational order and velocity field in the active nematic respectively and $\boldsymbol{u}$ the displacement field in the viscoelastic layers.

Active nematics may develop orientational order either due to the elongated shape of the constituents [47,48] or as an emergent feature of deformability of particles, such as cells [49] or due to activity itself [50]. The nematic order is measured using an orientational order parameter $\mathbf{Q} = 2q(\mathbf{nn} - \mathbf{I}/2)$, where $\mathbf{n} = [\cos(\theta), \sin(\theta)]$ is the director field, $\theta \in (-\pi/2, \pi/2)$ is the angle that the nematogens form with the positive-$x$ direction, $q$ is the magnitude of the nematic order, and $\mathbf{I}$ is the identity tensor. The nematic order parameter tensor evolves according to [51]

$$(\partial_t + \boldsymbol{v} \cdot \nabla)\mathbf{Q} = \mathbf{S} + \gamma^{-1}\mathbf{H}, \quad (1)$$

where $\mathbf{S} = 2\lambda q\boldsymbol{\mathcal{E}} + \boldsymbol{\Omega} \cdot \mathbf{Q} - \mathbf{Q} \cdot \boldsymbol{\Omega}$ describes the generalized corotational derivative, $\boldsymbol{\mathcal{E}} = [(\nabla\boldsymbol{v})^{\mathsf{T}} + (\nabla\boldsymbol{v})]/2$ is the strain rate tensor, and $\boldsymbol{\Omega} = [(\nabla\boldsymbol{v})^{\mathsf{T}} - (\nabla\boldsymbol{v})]/2$ is the vorticity tensor. The flow aligning parameter $\lambda$ is determined by the shape of the nematogens. In Eq. (1), $\gamma$ is the rotational viscosity and $\boldsymbol{H} = -\delta\mathcal{F}/\delta\boldsymbol{Q}$ is the molecular field which drives the system to the minimum of the free energy with energy density $\mathcal{F} = \frac{1}{2}A\boldsymbol{Q}^2 + \frac{1}{4}C\boldsymbol{Q}^4 + \frac{1}{2}K(\nabla\boldsymbol{Q})^2$. Here, $K$ is the elastic constant and $A$ and $C$ are material parameters, chosen so that the system is in the nematic phase at equilibrium.

The velocity field $\boldsymbol{v}$ obeys the incompressible Navier-Stokes equations [6,52]:

$$\nabla \cdot \boldsymbol{v} = 0, \quad \rho_1(\partial_t \boldsymbol{v} + \boldsymbol{v} \cdot \nabla\boldsymbol{v}) = \nabla \cdot \boldsymbol{\sigma}, \quad (2)$$

where the total stress tensor $\boldsymbol{\sigma}$ is given by the sum of (i) the viscous stress $\boldsymbol{\sigma}^{\text{viscous}} = 2\eta_1\boldsymbol{\mathcal{E}}$, where $\eta_1$ is the viscosity of the active nematic, (ii) the elastic stress $\boldsymbol{\sigma}^{\text{elastic}} = -P_1\boldsymbol{I} - 2\lambda q\boldsymbol{H} + \boldsymbol{Q} \cdot \boldsymbol{H} - \boldsymbol{H} \cdot \boldsymbol{Q}$, where $P_1$ is the bulk pressure, and (iii) the active stress $\boldsymbol{\sigma}^{\text{active}} = -\zeta\boldsymbol{Q}$. Here $\zeta$ is the activity

coefficient, with $\zeta > 0$ ($\zeta < 0$) corresponding to extensile (contractile) activity.

The dynamics of the incompressible viscoelastic layers is described by the displacement field $\boldsymbol{u}$ from the equilibrium position that evolves according to [53,54]

$$\nabla \cdot \boldsymbol{u} = 0, \quad \rho_2\frac{\partial^2 \boldsymbol{u}}{\partial t^2} = -\nabla P_2 + \nabla \cdot \boldsymbol{\tau}, \quad (3)$$

where $\rho_2$ is the gel density and $P_2$ is the bulk pressure in the viscoelastic layers. The stress tensor $\boldsymbol{\tau}$ is model dependent and we consider two simple yet powerful constitutive relations, namely

(i) Maxwell model:  $\dfrac{1}{E}\dfrac{D\boldsymbol{\tau}}{Dt} + \dfrac{1}{\eta_2}\boldsymbol{\tau} = \nabla\partial_t\boldsymbol{u} + (\nabla\partial_t\boldsymbol{u})^{\mathsf{T}}$,

(ii) Kelvin-Voigt model:  $\boldsymbol{\tau} = (E + \eta_2\partial_t)[\nabla\boldsymbol{u} + (\nabla\boldsymbol{u})^{\mathsf{T}}]$,

to capture the rheological response of the viscoelastic layers that confine the active nematic. In the above, $D/Dt$ is the upper convected derivative [54] and $E$ and $\eta_2$ are the elastic modulus and viscosity, respectively. A Maxwell (Kelvin-Voigt) material is composed of a spring and a dashpot connected in series (parallel). It behaves as an elastic solid at short (long) times and as a viscous liquid at long (short) times, with a single crossover timescale $\eta_2/E$.

Equations (1)–(3) govern the dynamics of the system and we solve them (i) analytically as a linear stability problem and (ii) numerically using a hybrid lattice Boltzmann method. We assume translational invariance in the $x$ direction, so that $v_y = 0$, $v_x = v_x(y)$ and $u_y = 0$, $u_x = u_x(y)$. The viscoelastic material is in contact with a no-slip wall at $y = \pm\beta L$. At the interface between the active nematics and the viscoelastic layer, we impose no-slip conditions, $v_x(\pm L) = \partial_t u_x(\pm L)$, and continuity of the stress tensor $\sigma_{xy}(\pm L) = \tau_{xy}(\pm L)$. For simplicity, we consider strong planar anchoring of the director field at the interface, i.e., $\theta(\pm L) = 0$.

## III. SPONTANEOUS OSCILLATIONS

To investigate the interplay of activity and viscoelasticity, we perform linear analysis to calculate the stability of a small perturbation around the static nematic state with $(v_x, u_x, \theta, q) = (0, 0, 0, q_0)$ where $q_0 = \sqrt{-A/(2C)}$. For each field, we consider small perturbations around the steady state $f_0$ of the type $f(y, t) = f_0 + \tilde{f}(y)e^{\omega t}$. In the limit of zero inertia ($\rho_1 = \rho_2 = 0$), the growth rate $\omega$ satisfies the transcendental equation (see Appendix A)

$$\frac{\omega + (\gamma^{-1}K\Lambda_1 - \omega/\Lambda_1)\tanh(\Lambda_1 L)}{[\eta_1\omega + q_0(1 - \lambda)\zeta]L} = \frac{(1 - \beta)}{E\mathcal{T}}, \quad (4)$$

where $\Lambda_1 = \sqrt{\dfrac{\eta_1\omega + q_0(1-\lambda)\zeta}{\eta_1\gamma^{-1}K + 2q_0^2K(\lambda-1)^2}}$. For Maxwell and Kelvin-Voigt models, respectively, $\mathcal{T} = (\omega + E/\eta_2)^{-1}$ and $\mathcal{T} = \omega^{-1} + \eta_2/E$. The nature of instability associated with the system depends on $\omega$—the solution of Eq. (4).

For simplicity, we first consider a purely elastic material bounding the nematic fluid, corresponding to the limit $\eta_2 \to \infty$ ($\eta_2 \to 0$) for the Maxwell (Kelvin-Voigt) model. In the limit of large elastic modulus $E \to \infty$, the boundaries at $y = \pm L$ are rigid and we recover the classical result of Voituriez *et al.* [2]: increasing the activity beyond a critical
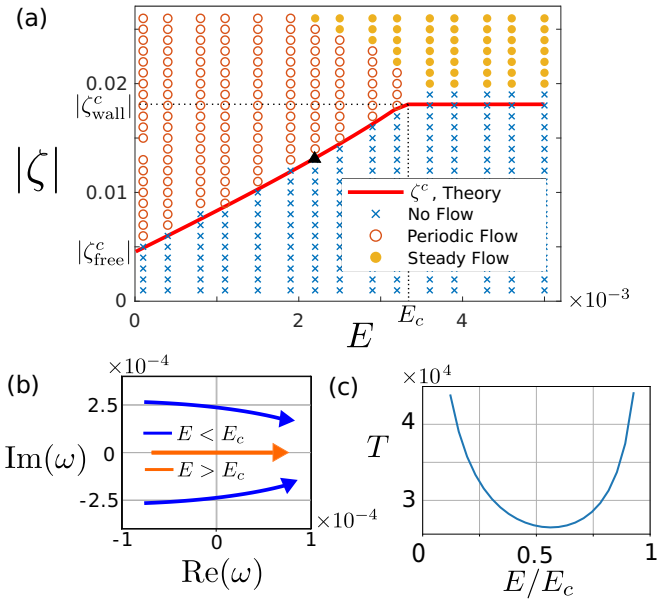
FIG. 2. (a) Phase diagram in the $(\zeta, E)$ plane, illustrating the states of an active nematic when confined in a purely elastic channel, corresponding to $\eta_2 = \infty$ ($\eta_2 = 0$) for the Maxwell (Kelvin-Voigt) model. The continuous red line is the critical activity $\zeta^c$, obtained from linear stability analysis, at which the nematic state becomes unstable, driving flows. The symbols are obtained from hybrid lattice Boltzmann simulations with $\eta_1 = 10/3$, $\gamma = 10$, $\rho_1 = 20$, $\rho_2 = 0$, $K = 0.1$, $q_0 = 0.25$, $L = 10$, $\lambda = 0$, and $\beta = 2$. For $E < E_c \approx 0.0033$, the instability leads to periodic oscillations. For $E > E_c$, a steady flow of active nematic is obtained. (b) The growth rate $\omega$ in the complex plane, for $E = 0.002 < E_c$ (blue lines) and $E = 0.0042 > E_c$ (orange line). The arrows indicate the direction of increasing $|\zeta|$. (c) Time period of oscillations $T$ as a function of $E/E_c$. $T$ diverges when $E \to 0$ and $E \to E_c$.

value $\zeta_{\text{wall}}^c$, the nematically ordered state is unstable and spontaneous flows develop driven by the distortions in the director field. The critical activity is calculated from Eq. (4),

$$\zeta_{\text{wall}}^c = -\frac{\pi^2 K \left[\eta_1/\gamma + 2q_0^2(1-\lambda)^2\right]}{q_0(1-\lambda)L^2}. \quad (5)$$

In the opposite limit $E = 0$, corresponding to a free-standing film of active nematic, an analogous transition to a steady flow is observed at activity $\zeta_{\text{free}}^c = \zeta_{\text{wall}}^c/4$.

The critical activity of the system at intermediate values of $E$, obtained from Eq. (4), is summarized in Fig. 2 (red line). The critical activity $\zeta^c = \zeta_{\text{free}}^c$ at $E = 0$ and nonlinearly (see Appendix B) increases with increase in the elastic modulus $E$, until a threshold elastic modulus $E = E_c$. Beyond $E_c$ the critical activity "freezes" to $\zeta^c = \zeta_{\text{wall}}^c$—that corresponding to a rigid wall.

Interestingly the transition mechanism at $\zeta^c$, at which the ordered nematic state becomes unstable, is different for $E < E_c$ and $E > E_c$. We find that, for $E < E_c$, the route to instability is via a Hopf bifurcation where the complex conjugate eigenvalues $\omega$ cross the imaginary axis with a finite imaginary part at $\zeta = \zeta^c$ [Fig. 2(b)]. Consequently, the ensuing instability is oscillatory and the active nematic transitions from a quiescent to an oscillating state where the flow
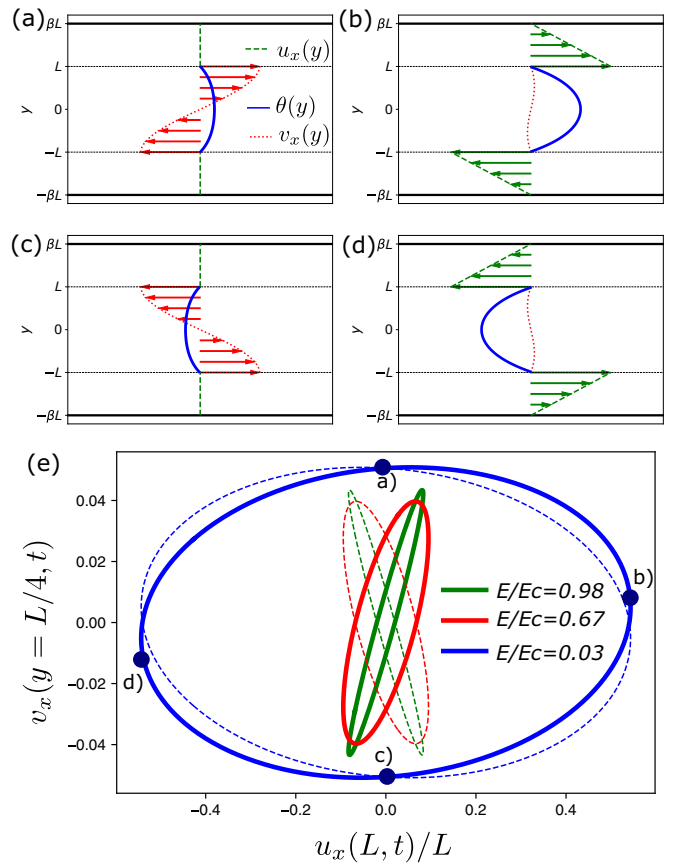


FIG. 3. Temporal evolution of the system with the same parameter values as in Fig. 2 at $\zeta = \zeta^c(E)$. The panels (a), (b), (c), and (d) show the hydrodynamic fields in the oscillatory phase for $t = 0$, $T/4$, $T/2$, $3T/4$. Panel (e) shows the phase space trajectory in the $[u_x(L, t), v_x(L/4, t)]$ plane for different values of $E$. The dashed lines display the time-reversed trajectories, showing time irreversibility.

direction is reversed periodically. On the other hand, for $E > E_c$, the instability becomes stationary [$\text{Im}(\omega) = 0$] and no oscillations are observed. The numerical simulations show that the oscillations are replaced by steady flow at sufficiently high activity (see Fig. 2).

The oscillatory state can be understood by following the temporal evolution of a system which is at its critical activity $\zeta = \zeta^c$ and with $0 < E < E_c$ and $|\zeta_{\text{free}}^c| < |\zeta| < |\zeta_{\text{wall}}^c|$ [such as a point marked "▲" in Fig. 2(a)]. At time $t = 0$ [see Fig. 3(a)], the elastic layer is not deformed ($u_x = 0$) and the stress at the active nematic-elastic interface ($y = \pm L$) vanishes. This condition corresponds to a freestanding active nematic film (no resistance from the elastic layer), which will have a critical activity $\zeta_{\text{free}}^c$. Since the activity of the system exceeds this critical value, $|\zeta| > |\zeta_{\text{free}}^c|$, spontaneous flow develops in the active film. The velocity profile $\tilde{v}_x(y)$ is an odd function of $y$ similar to that of a shear flow (see Appendix A). These flows, in turn, drive the deformation of the elastic confinement. Eventually, the elastic response of the channel wall slows down the flow and the deformation rate at the active-elastic interface vanishes. In this configuration, the effect of elastic confinement is the same as that of a rigid wall and the critical activity for the active nematic is

$\zeta_{\text{wall}}^c$. However, since $|\zeta| < |\zeta_{\text{wall}}^c|$, the active forcing is not sufficient to sustain the flows and they die out [Fig. 3(b)]. The elastic energy stored in the elastic medium pushes the flow in the opposite direction, leading to a flow reversal [Fig. 3(c)]. Hence the oscillations arise because the activity is too high to remain in the quiescent state ($\zeta > \zeta_{\text{free}}^c$) but too low to sustain the flow ($\zeta < \zeta_{\text{wall}}^c$). Note that, while the frequency of the oscillations depends on the material density, the critical value $\zeta^c(E)$ is independent of $\rho_1$ and $\rho_2$ (see Appendix A).

The critical elasticity $E_c$ can be computed analytically. Neglecting the elastic component of the stress in (2), we find (see Appendix B)

$$E_c \approx \frac{2\pi^2}{3} \frac{(\beta - 1)\eta_1 K}{\gamma L^2}. \quad (6)$$

Interestingly, the range of values of $E$ for which oscillations are observed can be extended by increasing the relative width $\beta$ of the elastic layer or decreasing the width $L$ of the sample. Using the values recently measured for tubulin-kinesin active nematic gel, we find $E_c L^2/(\beta - 1) \approx 3.9 \times 10^{-15}$ N m [55,56]. For $L \approx 50$ microns and height (in the direction perpendicular to the $x-y$ plane) $\Delta z \approx 0.5$ microns, we predict that for $\beta \approx 6$ the elastic inclusions developed in [56] would lead to oscillations (see Appendix B for details).

The period $T$ of the oscillations is set by the elasticity, viscosity, and $L/(\gamma^{-1}K)$—the relaxation timescale of the director field. The period $T$ close to the critical point $\zeta = \zeta^c$ can be obtained analytically from Eq. (4) (see Appendix A) and is shown in Fig. 2(c) as a function of $E$. For $E \to 0$, the activity $\zeta$ is only slightly larger than $\zeta_{\text{free}}^c$ required to initially start a flow, leading to a slowdown of the dynamics. Similarly, when $E \to E_c$, the activity $\zeta$ is only marginally below $\zeta_{\text{wall}}^c$ and the flow-reversal mechanism again slows down significantly. Indeed the time period diverges in the limiting cases: $T \sim \sqrt{\frac{L^2\eta_1}{\gamma^{-1}KE}}$ for $E \to 0$ and $\sqrt{\frac{L^2\eta_1}{\gamma^{-1}K(E_c-E)}}$ for $E \to E_c$. Hence the crossover from oscillatory to steady flow at the two limiting cases, $E > 0$ to $E = 0$ and $E < E_c$ to $E = E_c$, occurs smoothly via an infinite-period bifurcation. The period $T$ has a minimum at $E = E^*$, reminiscent of the phenomenon of resonance and the elastic modulus can be optimally tuned to increase the frequency of oscillatory motion.

To gain further insight into the oscillatory modes of the instability, we next plot the trajectory of the system in a phase space spanned by the displacement of the elastic layer $[u_x(y = L, t)]$ and the velocity of the active nematic $[v_x(y = L/4, t)]$ as shown in Fig. 3(e). The exact shape of the curve depends on the choice of parameters, but note that the phase space trajectory encloses a finite area indicating the phase lag in the velocity field of active nematic and the displacement field of elastic confinement. Interestingly, the phase space trajectory does not coincide with the time-reversed trajectory $[u_x(L, -t), -v_x(L/4, -t)]$, manifestly breaking the time-reversal symmetry and showing the nonequilibrium nature of the active-dissipative system under consideration. While nonreciprocal oscillatory motion, the sine qua non for self-propulsion (the scallop theorem), is abundant in life at low Reynolds number [57,58], the current analysis demonstrates that the mechanical coupling of activity and elasticity automatically generates such nonreciprocal motion in active systems.

Having established that the genesis of oscillations is the elasticity of the confining channel we can analyze more complex constitutive relations. For the Maxwell model, on timescales smaller than $\eta_2/E$ the viscoelastic confinement behaves as an elastic solid and the coupling between activity and elasticity still leads to oscillations as illustrated in Fig. 4(a). The instability becomes stationary for $E > E_c$ but with the difference that $E_c$ depends on the viscosity ratio $\eta_r = \eta_2/\eta_1$. When $E > E_c$, the viscoelastic confining material essentially behaves as a viscous fluid with critical activity $\zeta_{\text{visc}}^c$. Hence the critical activity $\zeta^c = \zeta_{\text{visc}}^c$ depends upon the viscosity ratio $\eta_r$ and $|\zeta_{\text{free}}^c| < |\zeta_{\text{visc}}^c| < |\zeta_{\text{wall}}^c|$. The behavior at small $E$ can be understood in a similar fashion. In this limit, the viscoelastic timescale $\eta_2/E$ is large compared to the period of the oscillations $T \sim 1/\sqrt{E}$ and the Maxwell material behaves as an elastic solid exhibiting an $\eta_r$ independent behavior of $\zeta^c$. In particular, $\zeta^c \approx \zeta_{\text{free}}^c$ at small elasticity $E$.

Opposite behaviors are observed when the channel confinement is the Kelvin-Voigt material. For $E > E_c$ the instability is still stationary but the confining material behaves as an elastic solid and $\zeta^c = \zeta_{\text{wall}}^c$; see Appendix C. This results in the threshold elastic modulus $E_c$ being independent of the viscosity $\eta_2$; see Fig. 4(b). For $E \to 0$, the viscoelastic timescale $\eta_2/E$ is large compared to the period of the oscillations and the Kelvin-Voigt material behaves as a viscous fluid. Hence the critical activity $\zeta^c$ for small $E$ strongly depends on $\eta_r$. To summarize, the choice of different constitutive models
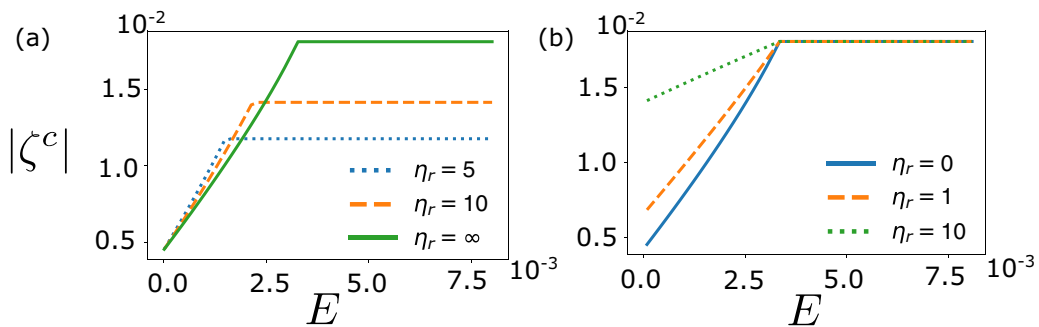


FIG. 4. Critical activity $|\zeta^c|$ as a function of the elastic modulus $E$ for different values of $\eta_r = \eta_2/\eta_1$ for the Maxwell model (a) and the Kelvin Voigt model (b). The values of the parameters are $\eta_1 = 10/3$, $\gamma = 10$, $\rho_1 = \rho_2 = 20$, $K = 0.1$, $q_0 = 0.25$, $L = 10$, $\lambda = 0$, and $\beta = 2$. In the regions where $|\zeta^c|$ increases with $E$ the instability is oscillatory.

of the channel confinement leads to quantitative differences but does not change the physics of the oscillations.

## IV. CONCLUSIONS

Our results highlight a pathway to spatiotemporal pattern formation in active matter in a minimal setting. It is indeed remarkable to note that the time periodic, oscillatory flows arise even at constant activity. Our predictions can be tested experimentally, by confining cell layers [5] or microtubule-based active fluids [25,56] in channels with soft walls. Moreover, traction force microscopy provides a potential platform to study the role of an active-elastic boundary [17,18]. Recent experiments have shown that active matter can be controlled in space by tuning the geometry of the confinement [29,34,35].

However, a precise criterion for temporal control is still missing [41]. In this paper, we have shown that for soft channels the temporal frequency $\omega$ of the system is coupled to the elastic constant $E$ of the material as $\omega \sim \sqrt{E}$. Therefore, tuning the mechanical properties of the surroundings, e.g., using light-activated inclusions [56], allows one to precisely control the temporal behavior of the system, with a variety of applications from microfluidics to soft robotics.

## APPENDIX A: LINEAR STABILITY ANALYSIS

In this section, we perform the linear stability analysis of Eqs. (1)–(3). Under the assumption of translational invariance in the $x$ direction, the governing equations for the nematic region ($|y| < L$) become

$$\partial_t q = \gamma^{-1}\{-q[A + 2Cq^2 - \gamma\lambda \sin(2\theta)\partial_y v_x + 4K(\partial_y\theta)^2] + K\partial_y^2\theta\},$$

$$\partial_t \theta = 2\gamma^{-1}Kq^{-1}\partial_y q\partial_y\theta + \tfrac{1}{2}\gamma^{-1}\{\gamma\partial_y v_v[\lambda \cos(2\theta) - 1] + 2K\partial_y^2\theta\},$$

$$\rho_1\partial_t v_x = \partial_y\sigma_{xy}, \tag{A1}$$

where

$$\sigma_{xy} = -2\lambda q\{\sin(2\theta)q[-A - 2B \cos^2(2\theta)q^2] + K[4\partial_y q\partial_y\theta \cos(2\theta) - 4q \sin(2\theta)(\partial_y\theta)^2]\} + 4Kq[2\partial_y q\partial_y\theta + q\partial_y^2\theta]$$

$$+ \eta_1\partial_y v_x - \zeta q \sin(2\theta). \tag{A2}$$

In the viscoelastic region ($y > |L|$), we find

$$\rho_2\partial_t^2 u_x = \partial_y\tau_{xy},$$

$$\frac{1}{E}\frac{D\tau_{xy}}{Dt} + \frac{1}{\eta_2}\tau_{xy} = \partial_y\partial_t u_x, \tag{A3}$$

where $D\tau_{xy}/(Dt) = \partial_t\tau_{xy} - \tau_{yy}\partial_y\partial_t u_x$ is the upper-convected derivative of the stress tensor. The boundary conditions are

$$\theta(y = \pm L) = 0, \quad v_x(y = \pm L) = \partial_t u_x(y = \pm L),$$

$$\tau_{xy}(\pm L) = \sigma_{xy}(\pm L), \quad u_x(\pm\beta L) = 0. \tag{A4}$$

We probe the stability of a small perturbation around the stationary state $(v_x, u_x, \theta, q) = [0, 0, 0, q_0 = \sqrt{-A/(2C)}]$ of the type $f(y, t) = f_0 + \tilde{f}(y)e^{\omega t}$. Expanding to linear order, we find

$$\omega\tilde{\theta} = \gamma^{-1}K\partial_y^2\tilde{\theta} + \frac{\lambda - 1}{2}\partial_y\tilde{v}_x,$$

$$\rho_1\omega\tilde{v}_x = \partial_y\sigma_{xy}, \tag{A5}$$

where

$$\sigma_{xy} = \eta_1\partial_y\tilde{v}_x - 2\zeta q_0\tilde{\theta} - 4q_0^2K(\lambda - 1)\partial_y^2\tilde{\theta} \tag{A6}$$

and

$$\partial_y^2\tilde{u}_x = \delta^2\tilde{u}_x, \tag{A7}$$

where

$$\delta = \sqrt{\rho_2\omega\left(\frac{\omega}{E} + \frac{1}{\eta_2}\right)}. \tag{A8}$$

The boundary conditions are

$$\eta_1\partial_y\tilde{v}_x(\pm L) - 2\zeta q_0\tilde{\theta}(\pm L) - 4q_0^2K(\lambda - 1)\partial_y^2\tilde{\theta}(\pm L)$$

$$= \frac{\omega}{\omega/E + 1/\eta_2}\partial_y\tilde{u}_x(\pm L), \tag{A9}$$

$$\tilde{\theta}(\pm L) = 0, \quad \tilde{v}_x(\pm L) = \omega\tilde{u}_x(\pm L), \quad \tilde{u}_x(\pm\beta L) = 0. \tag{A10}$$
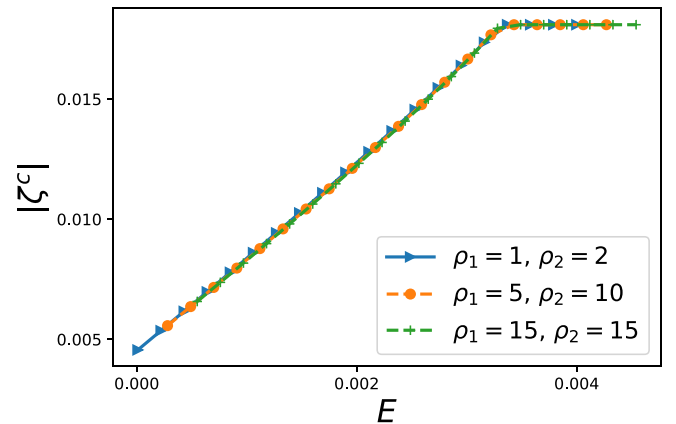


FIG. 5. Critical activity $\zeta^c$ as a function of $E$ for $\eta_1 = 10/3$, $\eta_2 = \infty$, $\gamma = 10$, $K = 0.1$, $q_0 = 0.25$, $L = 10$, $\lambda = 0$, $\beta = 2$, and different values of the densities $\rho_1$ and $\rho_2$.

Solving the gel equation (A7) and imposing the no-slip boundary condition $\tilde{u}_x(\pm\beta L) = 0$ we find

$$u_x(y) = c_4^{\pm}[\sinh(\delta y) \mp \tanh(\delta\beta L)\cosh(\delta y)], \quad \text{(A11)}$$

for $y > L$ ($y < -L$). From Eq. (A6), we obtain

$$\partial_y^4\tilde{\theta}(y) - a\partial_y^2\tilde{\theta}(y) + b\tilde{\theta}(y) = 0, \quad \text{(A12)}$$

where we have defined

$$a = \frac{\eta_1\omega + \gamma^{-1}K\rho_1\omega - q_0\zeta(\lambda - 1)}{\eta_1\gamma^{-1}K + 2q_0^2K(\lambda - 1)^2} \quad \text{(A13)}$$

and

$$b = \frac{\rho_1\omega^2}{\eta_1\gamma^{-1}K + 2q_0^2K(\lambda - 1)^2}. \quad \text{(A14)}$$

We first consider the even solution

$$\theta(y) = c_1\left[\cosh(\Lambda_1 y) - \frac{\cosh(\Lambda_1 L)}{\cosh(\Lambda_2 L)}\cosh(\Lambda_2 y)\right], \quad \text{(A15)}$$

where we have imposed the boundary condition $\theta(\pm L) = 0$ and defined

$$\Lambda_{1,2} = \sqrt{\frac{a \pm \sqrt{a^2 - 4b}}{2}}. \quad \text{(A16)}$$

Using Eq. (A5), we find

$$\tilde{v}_x(y) = \frac{2}{1-\lambda}c_1\left[\left(\gamma^{-1}K\Lambda_1 - \frac{\omega}{\Lambda_1}\right)\sinh(\Lambda_1 y) - \left(\gamma^{-1}K\Lambda_2 - \frac{\omega}{\Lambda_2}\right)\frac{\cosh(\Lambda_1 L)}{\cosh(\Lambda_2 L)}\sinh(\Lambda_2 y)\right]. \quad \text{(A17)}$$

Imposing the boundary conditions at $y = \pm L$, we find the following condition for $\omega$:

$$\frac{(\gamma^{-1}K\Lambda_1 - \omega/\Lambda_1)\tanh(\Lambda_1 L) - (\gamma^{-1}K\Lambda_2 - \omega/\Lambda_2)\tanh(\Lambda_2 L)}{(\Lambda_1^2 - \Lambda_2^2)[\gamma^{-1}\eta_1 K + 2q_0^2K(1-\lambda)^2]} + \left(\frac{\omega}{E} + \frac{1}{\eta_2}\right)\frac{\tanh[\delta(\beta-1)L]}{\delta} = 0. \quad \text{(A18)}$$

Considering the odd solution, we find

$$\theta(y) = c_1\left[\sinh(\Lambda_1 y) - \frac{\sinh(\Lambda_1 L)}{\sinh(\Lambda_2 L)}\sinh(\Lambda_2 y)\right], \quad \text{(A19)}$$

$$\tilde{v}_x(y) = \frac{2}{1-\lambda}c_1\left[\left(\gamma^{-1}K\Lambda_1 - \frac{\omega}{\Lambda_1}\right)\cosh(\Lambda_1 y) - \left(\gamma^{-1}K\Lambda_2 - \frac{\omega}{\Lambda_2}\right)\frac{\sinh(\Lambda_1 L)}{\sinh(\Lambda_2 L)}\cosh(\Lambda_2 y)\right], \quad \text{(A20)}$$

and the condition

$$\frac{(\gamma^{-1}K\Lambda_1 - \omega/\Lambda_1)\coth(\Lambda_1 L) - (\gamma^{-1}K\Lambda_2 - \omega/\Lambda_2)\coth(\Lambda_2 L)}{(\Lambda_1^2 - \Lambda_2^2)[\gamma^{-1}\eta_1 K + 2q_0^2K(1-\lambda)^2]} + \left(\frac{\omega}{E} + \frac{1}{\eta_2}\right)\frac{\tanh[\delta(\beta-1)L]}{\delta} = 0. \quad \text{(A21)}$$

For the range of parameters considered in the paper, we find that the even solution (corresponding to no net flow in the channel) is dominant, i.e., it becomes unstable at lower values of the activity. Hence, in the main text, we only focus on the even mode. The odd solutions may be favored by introducing weak anchoring. In Fig. 5 we show that the critical value $\zeta^c$ of the activity is independent of the densities $\rho_1$ and $\rho_2$.

## APPENDIX B: ASYMPTOTIC BEHAVIORS

In this section, we extract the asymptotic behavior of the solution of Eq. (A18). For simplicity, we consider the case $\rho_1 = \rho_2 = 0$. In this limit, the condition in Eq. (A18) becomes

$$\frac{\omega L + (\gamma^{-1}K\Lambda_1 - \omega/\Lambda_1)\tanh(\Lambda_1 L)}{\eta_1\omega + (1-\lambda)q_0\zeta} + \left(\frac{\omega}{E} + \frac{1}{\eta_2}\right)(\beta-1)L = 0, \quad \text{(B1)}$$

where

$$\Lambda_1 = \sqrt{\frac{\eta_1\omega + q_0(1-\lambda)\zeta}{\eta_1\gamma^{-1}K + 2Kq_0^2(\lambda-1)^2}}. \quad \text{(B2)}$$

We first consider the limit of small $E$. For $E = 0$ (corresponding to a free surface), the critical value of the activity can be computed analytically and reads

$$\zeta_{\text{free}}^c = -\pi^2\frac{\eta_1\gamma^{-1}K + 2Kq_0^2(1-\lambda)^2}{4q_0L^2(1-\lambda)}. \quad \text{(B3)}$$

We set $E = \epsilon$, $\zeta = \zeta_{\text{free}}^c + a_1\epsilon$, and $\omega = a_2\sqrt{\epsilon}$. We then expand Eq. (B1) in powers of $\epsilon$, yielding

$$\frac{a_2L(-1+\beta) + \frac{2K}{a_2\gamma L\eta_1}}{\sqrt{\epsilon}} + \left[\frac{L(-1+\beta)}{\eta_2} + \frac{2L[5\eta_1 + 8\gamma q_0^2(1-\lambda)^2]}{\pi^2\eta_1[\eta_1 + 2q_0^2\gamma(1-\lambda)^2]} + \frac{2a_1Kq_0(-1+\lambda)}{a_2^2L\gamma\eta_1^2}\right] + \mathcal{O}(\sqrt{\epsilon}) = 0. \quad \text{(B4)}$$

Setting the coefficients to zero, we get

$$a_2 = \pm i \frac{\sqrt{2\gamma^{-1}K}}{L\sqrt{\eta_1(\beta-1)}} \tag{B5}$$

and

$$a_1 = -\frac{1}{q_0(1-\lambda)}\left[\frac{\eta_1}{\eta_2} + \frac{2[5\eta_1 + 8q_0^2\gamma(1-\lambda)^2]}{\pi^2(\beta-1)[\eta_1 + 2q_0^2\gamma(1-\lambda)^2]}\right]. \tag{B6}$$

As expected, the growth rate $\omega$ is purely imaginary. Using the parameters of Fig. 2, we find $a_1 \approx -3.83$.

To investigate the asymptotic behavior of the system close to the transition, we set $E = E_c - \epsilon$, $\zeta = \zeta_{\text{visc}}^c - a_1\epsilon$, and $\omega = a_2\sqrt{\epsilon}$, yielding

$$\left[\frac{L(\beta-1)}{\eta_2} - \frac{K\sqrt{-\frac{q_0\gamma\zeta_{\text{visc}}^c(-1+\lambda)}{K[\eta_1+2q_0^2\gamma(-1+\lambda)^2]}}\tanh\left(L\sqrt{-\frac{q_0\gamma\zeta_{\text{visc}}^c(-1+\lambda)}{K[\eta_1+2q_0^2\gamma(-1+\lambda)^2]}}\right)}{-\gamma\zeta_{\text{visc}}^c + \gamma\zeta_{\text{visc}}^c\lambda}\right]$$

$$+ \left[\frac{[a_2L(-1+\beta)]}{E_c} - \frac{a_2[3\eta_1+4q_0^2\gamma(-1+\lambda)^2]}{2\zeta_{\text{visc}}^c[\eta_1+2q_0^2\gamma(-1+\lambda)^2](-1+\lambda)} + \frac{a_2\eta_1 L \tanh\left(L\sqrt{-\frac{q_0\gamma\zeta_{\text{visc}}^c(-1+\lambda)}{K[\eta_1+2q_0^2\gamma(-1+\lambda)^2]}}\right)^2}{2q_0\zeta_{\text{visc}}^c[\eta_1+2q_0^2\gamma(-1+\lambda)^2](-1+\lambda)}\right.$$

$$\left. - \frac{a_2K[3\eta_1+4q_0^2\gamma(-1+\lambda)^2]\sqrt{-\frac{q_0\gamma\zeta_{\text{visc}}^c(-1+\lambda)}{K[\eta_1+2\gamma q_0^2(-1+\lambda)^2]}}\tanh\left(L\sqrt{-\frac{q_0\gamma\zeta_{\text{visc}}^c(-1+\lambda)}{K[\eta_1+2q_0^2\gamma(-1+\lambda)^2]}}\right)}{2q_0^2\gamma\left(\zeta_{\text{visc}}^c\right)^2(-1+\lambda)^2}\right]\sqrt{\epsilon} + \mathcal{O}(\epsilon) = 0. \tag{B7}$$

Setting the coefficients to zero we find

$$\frac{L(\beta-1)}{\eta_2} - \frac{K\sqrt{-\frac{q_0\gamma\zeta_{\text{visc}}^c(-1+\lambda)}{K[\eta_1+2q_0^2\gamma(-1+\lambda)^2]}}\tanh\left(L\sqrt{-\frac{q_0\gamma\zeta_{\text{visc}}^c(-1+\lambda)}{K[\eta_1+2q_0^2\gamma(-1+\lambda)^2]}}\right)}{-\gamma\zeta_{\text{visc}}^c + \gamma\zeta_{\text{visc}}^c\lambda} = 0 \tag{B8}$$

and $E_c$ can be simply obtained by setting to zero the coefficient of $\sqrt{\epsilon}$. Equation (B8) is transcendental and must be solved numerically to determine $\zeta_{\text{visc}}^c$. Considering higher order expansions, one can find expressions for $a_1$ and $a_2$. In particular, using the parameter values from Fig. 2 we find that the slope of $\zeta$ at $E = E_c$ is $a_1 \approx 4.79$. Thus the slopes of $\zeta$ as a function of $E$ at $E = 0$ and $E = E_c$ differ, implying that $\zeta$ is not a linear function of $E$, as shown in Fig. 6.

In the limit of a purely elastic medium ($\eta_2 \to \infty$) we find

$$E_c = \frac{2K\pi^2(-1+\beta)[\eta_1+2q_0^2\gamma(-1+\lambda)^2]^2}{L^2\gamma[3\eta_1+4q_0^2\gamma(-1+\lambda)^2]}. \tag{B9}$$

Finally, neglecting the elastic component of the nematic stress, we obtain

$$E_c \approx \frac{2\pi^2}{3}\frac{(\beta-1)\eta_1 K}{\gamma L^2}. \tag{B10}$$

We next focus on tubulin-kinesin active nematic gels [47], for which neglecting the elastic component of the stress is justified by experimental measurements [56]. In Ref. [56], experiments with microfabricated elastic inclusions lead to the estimates $K \approx 6 \times 10^{-16}$ N m and $\eta_1 \approx 10^{-5}$ Pa s m. Taking

$\gamma \approx \eta_1$ [55], we get

$$\frac{E_c L^2}{\beta-1} \approx 3.9 \times 10^{-15} \text{ N m}. \tag{B11}$$

We consider a substrate of width $L \approx 50$ microns and height (in the direction perpendicular to the $x-y$ plane) $\Delta z = 0.5$ microns. In [56], the 3D elastic constant of the elastic inclusions was measured to be $E^{\text{3D}} = E/\Delta z \approx 18$ Pa. Therefore, our model predicts that for $\beta \approx 6$ oscillations would be observed.

## APPENDIX C: KELVIN-VOIGT MODEL

In this section, we perform the linear stability analysis in the case of the Kelvin-Voigt model. The constitutive relation reads

$$\tau_{xy} = (E + \eta_2\partial_t)\partial_y u_x. \tag{C1}$$

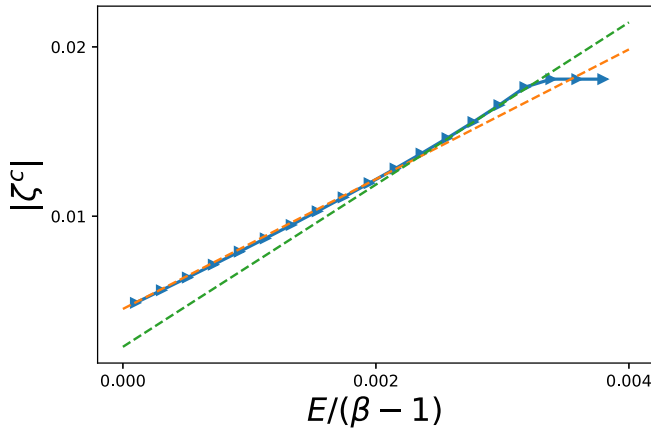FIG. 6. Critical activity $\zeta^c$ as a function of $E$ for the same parameter values as in Fig. 2. The dashed lines show the exact asymptotic behaviors derived for $E \to 0$ and $E \to E_c$. The critical activity $\zeta_c$ is constant for $E > E_c$.

Hence the gel displacement $u_x(y, t)$ evolves according to

$$\rho_2 \partial_t^2 u_x = (E + \eta_2 \partial_t) \partial_y^2 u_x. \qquad (C2)$$

Assuming $u_x(y, t) = e^{\omega t} \tilde{u}_x(y)$, we find

$$\partial_y^2 \tilde{u}_x = \delta_{KV}^2 \tilde{u}_x, \qquad (C3)$$

where we have defined

$$\delta_{KV} = \sqrt{\frac{\rho_2 \omega^2}{E + \eta_2 \omega}}. \qquad (C4)$$

Following the same derivation as for the Maxwell model, we find two instabilities, corresponding to the even and odd solutions for $\theta$. The condition for the growth rate of the even solution reads

$$\frac{(\gamma^{-1} K \Lambda_1 - \omega/\Lambda_1) \tanh(\Lambda_1) - (\gamma^{-1} K \Lambda_2 - \omega/\Lambda_2) \tanh(\Lambda_2)}{(\Lambda_1^2 - \Lambda_2^2)[\gamma^{-1} \eta_1 K + 2q_0 K(1 - \lambda)^2]}$$
$$+ \frac{\omega}{E + \omega \eta_2} \frac{\tanh[\delta_{KV}(\beta - 1)]}{\delta_{KV}} = 0. \qquad (C5)$$

For the odd solution, we find

$$\frac{(\gamma^{-1} K \Lambda_1 - \omega/\Lambda_1) \coth(\Lambda_1) - (\gamma^{-1} K \Lambda_2 - \omega/\Lambda_2) \coth(\Lambda_2)}{(\Lambda_1^2 - \Lambda_2^2)[\gamma^{-1} \eta_1 K + 2q_0 K(1 - \lambda)^2]}$$
$$+ \frac{\omega}{E + \omega \eta_2} \frac{\tanh[\delta_{KV}(\beta - 1)]}{\delta_{KV}} = 0. \qquad (C6)$$

As for the Maxwell model, for the range of parameters considered in the paper, we find that the even solution is dominant.

[1] M. E. Cates and J. Tailleur, Annu. Rev. Condens. Matter Phys. **6**, 219 (2015).

[2] R. Voituriez, J.-F. Joanny, and J. Prost, Europhys. Lett. **70**, 404 (2005).

[3] S. A. Edwards and J. M. Yeomans, Europhys. Lett. **85**, 18008 (2009).

[4] L. Giomi, L. Mahadevan, B. Chakraborty, and M. Hagan, Nonlinearity **25**, 2245 (2012).

[5] G. Duclos, C. Blanch-Mercader, V. Yashunsky, G. Salbreux, J.-F. Joanny, J. Prost, and P. Silberzan, Nat. Phys. **14**, 728 (2018).

[6] M. C. Marchetti, J.-F. Joanny, S. Ramaswamy, T. B. Liverpool, J. Prost, M. Rao, and R. A. Simha, Rev. Mod. Phys. **85**, 1143 (2013).

[7] S. P. Thampi and J. M. Yeomans, Eur. Phys. J.: Spec. Top. **225**, 651 (2016).

[8] R. Alert, J. Casademunt, and J.-F. Joanny, Annu. Rev. Condens. Matter Phys. **13**, 143 (2022).

[9] J. C. Conrad and R. Poling-Skutvik, Annu. Rev. Chem. Biomol. Eng. **9**, 175 (2018).

[10] P. Friedl and D. Gilmour, Nat. Rev. Mol. Cell Biol. **10**, 445 (2009).

[11] O. Chaudhuri, J. Cooper-White, P. A. Janmey, D. J. Mooney, and V. B. Shenoy, Nature (London) **584**, 535 (2020).

[12] A. G. Clark, A. Maitra, C. Jacques, M. Bergert, C. Pérez-González, A. Simon, L. Lederer, A. Diz-Muñoz, X. Trepat, R. Voituriez *et al.*, Nat. Mater. **21**, 1200 (2022).

[13] A. Elosegui-Artola, A. Gupta, A. J. Najibi, B. R. Seo, R. Garry, C. M. Tringides, I. de Lázaro, M. Darnell, W. Gu, Q. Zhou *et al.*, Nat. Mater. **22**, 117 (2023).

[14] R. Sunyer and X. Trepat, Curr. Biol. **30**, R383 (2020).

[15] A. Patteson, A. Gopinath, M. Goulian, and P. Arratia, Sci. Rep. **5**, 15761 (2015).

[16] A. Zöttl and J. M. Yeomans, Nat. Phys. **15**, 554 (2019).

[17] R. W. Style, R. Boltyanskiy, G. K. German, C. Hyland, C. W. MacMinn, A. F. Mertz, L. A. Wilen, Y. Xu, and E. R. Dufresne, Soft Matter **10**, 4047 (2014).

[18] H. Colin-York and M. Fritzsche, Curr. Opin. Biomed. Eng. **5**, 1 (2018).

[19] A. Brugués, E. Anon, V. Conte, J. H. Veldhuis, M. Gupta, J. Colombelli, J. J. Muñoz, G. W. Brodland, B. Ladoux, and X. Trepat, Nat. Phys. **10**, 683 (2014).

[20] K. Chiou and E.-M. S. Collins, Dev. Biol. **433**, 155 (2018).

[21] B. Weigelin, G.-J. Bakker, and P. Friedl, IntraVital **1**, 32 (2012).

[22] P.-G. De Gennes and J. Prost, *The Physics of Liquid Crystals* (Oxford University Press, Oxford, 1993), p. 83.

[23] M. Deforet, V. Hakim, H. Yevick, G. Duclos, and P. Silberzan, Nat. Commun. **5**, 3747 (2014).

[24] H. Wioland, E. Lushi, and R. E. Goldstein, New J. Phys. **18**, 075002 (2016).

[25] P. Chandrakar, M. Varghese, S. A. Aghvami, A. Baskaran, Z. Dogic, and G. Duclos, Phys. Rev. Lett. **125**, 257801 (2020).

[26] A. Singh, Q. Vagne, F. Jülicher, and I. F. Sbalzarini, Phys. Rev. Res. **5**, L022061 (2023).

[27] J. Hardoüin, R. Hughes, A. Doostmohammadi, J. Laurent, T. Lopez-Leon, J. M. Yeomans, J. Ignés-Mullol, and F. Sagués, Commun. Phys. **2**, 121 (2019).

[28] T. N. Shendruk, A. Doostmohammadi, K. Thijssen, and J. M. Yeomans, Soft Matter **13**, 3853 (2017).

[29] S. P. Thampi, Curr. Opin. Colloid Interface Sci. **61**, 101613 (2022).

[30] A. Opathalage, M. M. Norton, M. P. Juniper, B. Langeslay, S. A. Aghvami, S. Fraden, and Z. Dogic, Proc. Natl. Acad. Sci. USA **116**, 4788 (2019).

[31] S. Chandragiri, A. Doostmohammadi, J. M. Yeomans, and S. P. Thampi, Soft Matter **15**, 1597 (2019).

[32] A. Samui, J. M. Yeomans, and S. P. Thampi, Soft Matter **17**, 10640 (2021).

[33] C. Joshi, Z. Zarei, M. M. Norton, S. Fraden, A. Baskaran, and M. F. Hagan, arXiv:2304.04895.

[34] J. Hardoüin, J. Laurent, T. Lopez-Leon, J. Ignés-Mullol, and F. Sagués, Soft Matter **16**, 9230 (2020).

[35] J. Hardoüin, C. Doré, J. Laurent, T. Lopez-Leon, J. Ignés-Mullol, and F. Sagués, Nat. Commun. **13**, 6675 (2022).

[36] N. A. Araújo, L. M. Janssen, T. Barois, G. Boffetta, I. Cohen, A. Corbetta, O. Dauchot, M. Dijkstra, W. M. Durham, A. Dussutour *et al.*, Soft Matter **19**, 1695 (2023).

[37] F. Juelicher, K. Kruse, J. Prost, and J.-F. Joanny, Phys. Rep. **449**, 3 (2007).

[38] P. Marcq, Eur. Phys. J. E **37**, 29 (2014).

[39] G. Li and A. M. Ardekani, Phys. Rev. Lett. **117**, 118001 (2016).

[40] E. J. Hemingway, M. E. Cates, and S. M. Fielding, Phys. Rev. E **93**, 032702 (2016).

[41] S. Liu, S. Shankar, M. C. Marchetti, and Y. Wu, Nature (London) **590**, 80 (2021).

[42] E. M. de Kinkelder, E. Fischer-Friedrich, and S. Aland, New J. Phys. **25**, 053035 (2023).

[43] E. L. C. VI M. Plan, J. M. Yeomans, and A. Doostmohammadi, Phys. Rev. Fluids **5**, 023102 (2020).

[44] E. L. VI M. Plan, J. M. Yeomans, and A. Doostmohammadi, J. R. Soc. Interface **18**, 20210100 (2021).

[45] E. L. C. VI M. Plan, H. Le Thi, J. M. Yeomans, and A. Doostmohammadi, J. Phys. A: Math. Theor. **55**, 275601 (2022).

[46] A. E. Hamby, D. K. Vig, S. Safonova, and C. W. Wolgemuth, Sci. Adv. **4**, eaau0125 (2018).

[47] T. Sanchez, D. T. Chen, S. J. DeCamp, M. Heymann, and Z. Dogic, Nature (London) **491**, 431 (2012).

[48] J. Galanis, R. Nossal, W. Losert, and D. Harries, Phys. Rev. Lett. **105**, 168001 (2010).

[49] R. Mueller, J. M. Yeomans, and A. Doostmohammadi, Phys. Rev. Lett. **122**, 048004 (2019).

[50] S. Santhosh, M. R. Nejad, A. Doostmohammadi, J. M. Yeomans, and S. P. Thampi, J. Stat. Phys. **180**, 699 (2020).

[51] A. N. Beris and B. J. Edwards, *Thermodynamics of Flowing Systems: With Internal Microstructure* (Oxford University Press on Demand, 1994), p. 36.

[52] A. Doostmohammadi, J. Ignés-Mullol, J. M. Yeomans, and F. Sagués, Nat. Commun. **9**, 3246 (2018).

[53] L. D. Landau, E. M. Lifshitz, A. M. Kosevich, and L. P. Pitaevskii, *Theory of Elasticity: Volume 7* (Elsevier, Amsterdam, 1986).

[54] D. D. Joseph, *Fluid Dynamics of Viscoelastic Liquids* (Springer Science & Business Media, New York, 2013), Vol. 84.

[55] B. Martínez Prat, Ph.D. thesis, Universitat de Barcelona, 2022.

[56] I. Vélez-Cerón, P. Guillamat, F. Sagués, and J. Ignés-Mullol, arXiv:2307.11587.

[57] E. M. Purcell, Am. J. Phys. **45**, 3 (1977).

[58] E. Lauga, Soft Matter **7**, 3060 (2011).